Title

Deterministic multi-step rotation of magnetic single-domain state in Nickel nanodisks using multiferroic magnetoelastic coupling

Permalink

https://escholarship.org/uc/item/0gh8750x

Authors

Sohn, Hyunmin
Liang, Cheng-yen
Nowakowski, Mark E
et al.

Publication Date

2017-10-01

DOI

10.1016/j.jmmm.2017.04.077

Peer reviewed

Research articles

Deterministic multi-step rotation of magnetic single-domain state in Nickel nanodisks using multiferroic magnetoelastic coupling

Hyunmin Sohn [a], Cheng-yen Liang [b], Mark E. Nowakowski [c], Yongha Hwang [d], Seungoh Han [e], Jeffrey Bokor [c], Gregory P. Carman [b], Robert N. Candler [a,b,f,*]

[a] Department of Electrical Engineering, University of California, Los Angeles, CA 90095, USA
[b] Department of Mechanical and Aerospace Engineering, University of California, Los Angeles, CA 90095, USA
[c] Department of Electrical Engineering and Computer Sciences, University of California, Berkeley, CA 94720, USA
[d] Department of Electro-Mechanical Systems Engineering, Korea University, Seoul 02841, Republic of Korea
[e] Department of Robotics Engineering, Hoseo University, Asan-si 31499, Republic of Korea
[f] California NanoSystems Institute, Los Angeles, CA 90095, USA

ABSTRACT

We demonstrate deterministic multi-step rotation of a magnetic single-domain (SD) state in Nickel nanodisks using the multiferroic magnetoelastic effect. Ferromagnetic Nickel nanodisks are fabricated on a piezoelectric Lead Zirconate Titanate (PZT) substrate, surrounded by patterned electrodes. With the application of a voltage between opposing electrode pairs, we generate anisotropic in-plane strains that reshape the magnetic energy landscape of the Nickel disks, reorienting magnetization toward a new easy axis. By applying a series of voltages sequentially to adjacent electrode pairs, circulating in-plane anisotropic strains are applied to the Nickel disks, deterministically rotating a SD state in the Nickel disks by increments of 45°. The rotation of the SD state is numerically predicted by a fully-coupled micromagnetic/elastodynamic finite element analysis (FEA) model, and the predictions are experimentally verified with magnetic force microscopy (MFM). This experimental result will provide a new pathway to develop energy efficient magnetic manipulation techniques at the nanoscale.

© 2017 Elsevier B.V. All rights reserved.

1. Introduction

Ferromagnetic materials, traditionally used in memory applications [1,2], are being incorporated into a wider range of emerging applications, which include nanotweezers [3,4], microfluidics [5,6], and biomedical applications [7,8]. These newer applications exploit the favorable scalability of the permanent magnetic diploe due to its relatively large energy density [9], in addition to its compatibility in fluidic environments. Previously, two major approaches have been studied to adapt magnetism at the nanoscale/microscale: scaling current-based magnetic coils [10], and employing external magnetic fields [6,11]. However, Joule heating causes significant limitations in current-based magnetic devices, as devices are miniaturized below the microscale due to reduced efficiency and challenges of heat dissipation. Use of external magnetic field control requires external magnetic sources such as permanent magnets or electromagnetic coils, which do not provide control at

the individual element-level control and limit overall system scalability. Therefore, control of magnetism is one of the major challenges when scaling magnetic systems below the microscale.

Recently, a new indirect approach to control magnetism has been suggested: strain-mediated multiferroic heterostructures [12–16]. Strain-mediated multiferroic composites consist of piezoelectric and magnetoelastic materials that are coupled via strain transfer at their interfaces. Instead of using an electric current or an external magnetic field to manipulate magnetization in the material, multiferroic composites use a piezoelectrically generated strain to control magnetization in nano/microstructures [17–25]. However, since most of the previous studies adapted single crystal piezoelectric materials that generate strain along specific crystal directions [25,26], the control of magnetism was confined by the crystal directions, with a lack of isotropic controllability. More recently, researchers suggested a way to generate isotropic strains with surface patterned electrodes on polycrystalline piezoelectric materials [27–30]. However, experimental work is unavailable to verify this type of magnetization control on elements below the micron scale.

In this work, we fabricate multiferroic heterostructures of Ni nanodisks on a Lead Zirconate Titanate (PZT) polycrystalline substrate to control rotation of magnetic single-domain (SD) states in Ni nanodisks. An array of surface electrodes is patterned on top of the PZT substrate to generate anisotropic in-plane strains in steps of 45°. The PZT-induced strains and corresponding magnetoelastic behavior in the SD states are predicted by a finite element analysis (FEA) that combines Landau-Lifshitz-Gilbert micromagnetics and elastodynamics. Lastly, we experimentally verify the rotation of the SD states in Ni nanodisks with magnetic force microscopy (MFM).

2. Theory

SD states in thin film ferromagnetic disks are achievable when the devices are scaled to sub-micron length scales (Fig. 1). The critical size to form a SD state depends on the exchange length, saturation magnetization, and shape anisotropy of the material. For a 15 nm thick Ni disk, a SD state starts to form in disks with diameter less than 400 nm [32]. The SD state in thin film disks possesses several useful properties for magnetic applications. First, due to its homogeneous configuration of magnetization, the magnetic single-domain emits a stray magnetic field at opposing sides of the disk, creating a dipole field for interaction with the external environment (Fig. 1). Second, the ferromagnetic structures have non-volatile, spontaneous magnetization, which can serve as a constant magnetic source. In addition, due to its symmetric circular shape, the disk structure does not possess shape anisotropy in the azimuthal angle or any preferential easy axis in-plane. Therefore, we can achieve isotopic rotation of SD states in the disks.

The magnetic energies that influence the SD state in the Ni nanodisks are the magnetocrystalline energy, exchange energy, demagnetization energy, and magnetoelastic energy. In this study, Ni disks are deposited by electron-beam evaporation and form polycrystalline structures, which means the macroscopic magnetocrystalline anisotropy energy is negligible compared to the other energy terms [33]. Therefore, creation of a magnetic SD state in Ni disks can be determined by an energy minimization process and balance between the exchange energy and demagnetization energy. After applying a saturating magnetic field, the initial homogeneous magnetization in disk structures produces a large internal demagnetization field that tends to create multi-domains or a vortex state to reduce the large demagnetization energy, which comes with increase of the exchange energy. Below a certain size scale, the exchange energy dominates the demagnetization energy, reducing the favorability to form multi-domain states.

By applying strain to the SD states, we can reshape the energy landscape through control of the magnetoelastic energy. For polycrystalline thin film disks, we assume the in-plane isotropic magnetoelastic energy, which is given as

$$E_{m.e.} = -\frac{3}{2}\lambda_s E\left(s_x \cos^2\theta + s_y \sin^2\theta\right)$$
$$= -\frac{3}{2}\lambda_s E\left[(s_x - s_y)\cos^2\theta + s_y\right] \quad (1)$$

where λ_s is saturation magnetostriction, E is Young's modulus, θ is the angle between magnetization and strain, and s_x and s_y are strain in x, and y, respectively (Fig. 2a). If the applied strain provides sufficiently large energy to overcome the local energy barrier that is imposed by the current exchange energy and demagnetization energy, the magnetization realigns toward the new easy axis formed by the strain. To more effectively drive the SD states, we calculate the optimal control angle to apply a strain with respect to a magnetic single-domain. This is found by the magnetoelastic effective field,

$$\vec{H}_{m.e.} = -\frac{1}{\mu_0}\nabla E_{m.e.} = \frac{1}{\mu_0}\frac{1}{r}\frac{\partial}{\partial\theta}(-\nabla E_{m.e.})\cdot\widehat{\theta}$$
$$= -\frac{3}{2}\frac{1}{\mu_0}\frac{1}{r}\lambda_s E(s_x - s_y)\sin 2\theta\cdot\widehat{\theta} \quad (2)$$

This effective field is the local field that the disk experiences due to the applied strain. The magnetic effective field is a function of $(s_x - s_y)$ and $\sin 2\theta$. The maximum magnitudes of the field are at ±45°, or ±135°. In addition, the effective field can be increased by a larger strain difference, $(s_x - s_y)$. Therefore, applying different polarity of orthogonal strains $(s_x \cdot s_y < 0)$ at +45° or −45° toward a magnetic single-domain maximizes the initial effective field to overcome the local energy barrier and reorient the magnetization toward the new easy axis. For example, the magnetoelastic energy and magnetoelastic effective field for $(s_x - s_y) < 0$ and $\lambda_s < 0$ are shown in Fig. 2b. In this case, the minimum $E_{m.e.}$, or easy axis, is created along the x axis, and the maximum effective field is generated when magnetization with $\theta = \pm45, \pm135°$.

Additional rotation of the SD state beyond the initial 45° step requires the generation of strains in multiple angles. This is suggested by recent studies [27–30], which analytically simulated the generation of orthogonal localized strains on a 500 nm thick PZT film with six surface patterned electrodes [28]. When applying a 10 MV/m electric field between the electrode pair and bottom of the PZT film, ~1000 ppm of in-plane anisotropic strain is generated at the center of the top surface of the electrodes, enabling manipulation of the magnetic state in a single ring structure [28].

3. Results and discussions

In this study, we use 300 μm thick polycrystalline PZT substrates (PZT 610HD from TRS Technologies) and pattern eight surface electrodes on the substrate (Fig. 3a). The polycrystalline PZT substrates show negligible macroscopic crystalline anisotropy, so they are suitable to generate in-plane isotropic strains with the
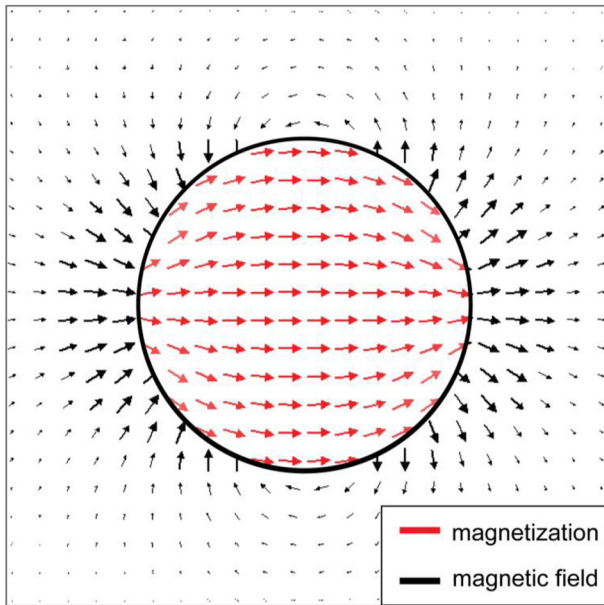
Fig. 1. Magnetic single-domain state in a Ni disk with thickness of 15 nm and diameter of 400 nm. The magnetic state is obtained using the Object Oriented MicroMagnetic Framework [31] (OOMMF) simulation tool. Nickel has saturation magnetization, Ms = 485 emu/cc, exchange constant, A = 9.0 × 10^{-12} J/m, and saturation magnetostriction, λ_s = −34 ppm. The Ni disk emits a maximum stray magnetic field of |Hmax| = 2.8 kOe.
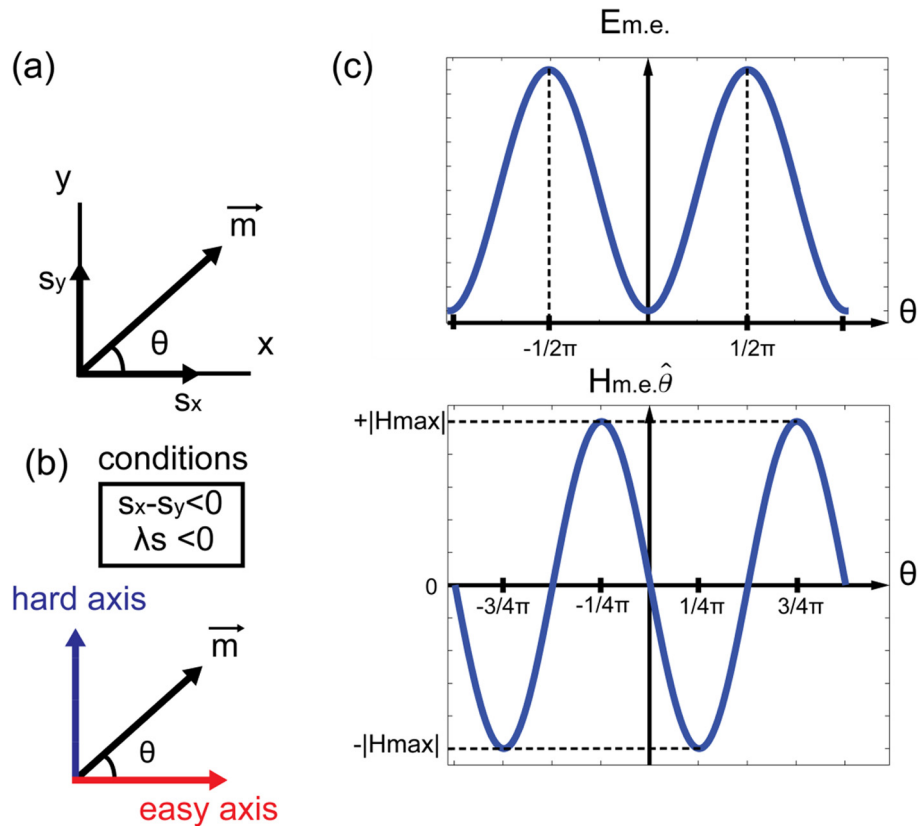
Fig. 2. Calculation of the optimal angle to apply strain for control of magnetization (a) Orientations of strain and magnetization (strain in the x axis (s_x), strain in the y axis (s_y), magnetization (m), and angle between s_x and m (θ)) (b) Orientations of the easy and hard axis when ($s_x - s_y$) < 0 and λ_s < 0. The easy and hard axis are created along the x and y axis, respectively (c) The magnetoelastic energy ($E_{m.e.}$) and magnetoelastic effective field ($H_{m.e.}$) for ($s_x - s_y$) < 0 and λ_s < 0. Magnetization at ±45° experiences the maximum effective field of $\mp|Hmax|\hat{\theta}$ toward the closest easy axis, the +x axis. As magnetization gets closer to the hard axis ($\theta = \pm 90°$) from ±45°, the effective field decreases, and the magnetization falls into a unstable equilibrium state ($E'_{m.e.} = 0$, $E''_{m.e.} < 0$) at the hard axis.
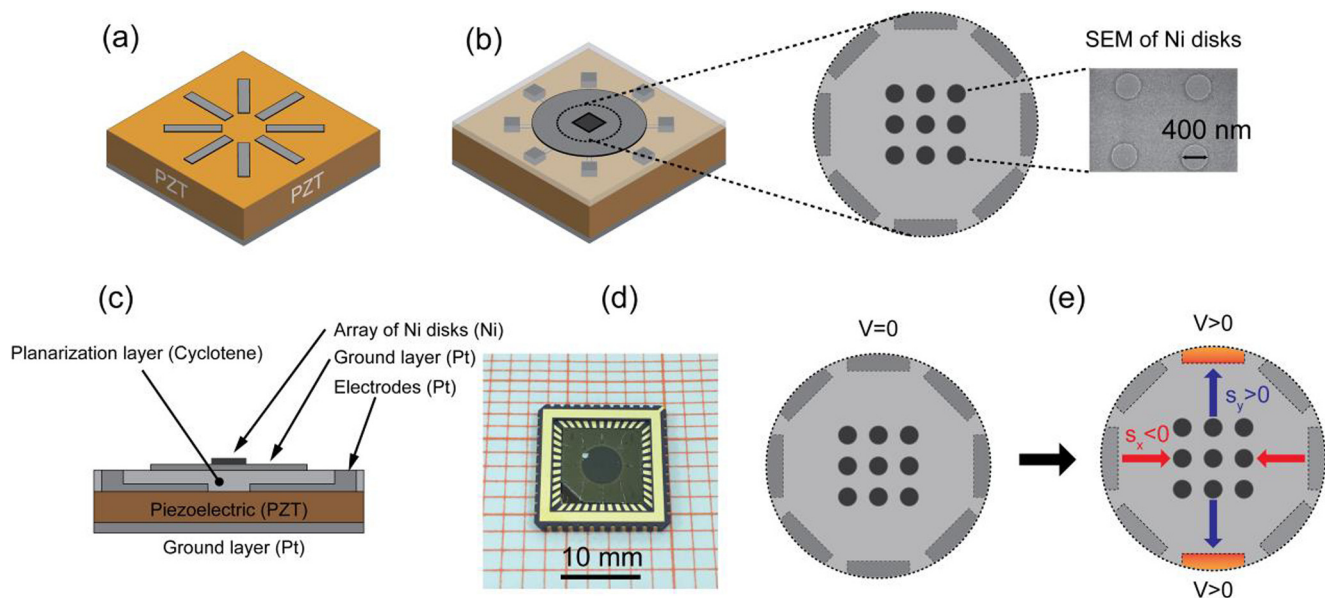
Fig. 3. Schematic of sample and generation of anisotropic in-plane strain. (a) Schematic of the PZT substrate with patterned electrodes. The top surface has 8 electrodes to generate anisotropic in-plane strains in steps of 45°. The backside of the PZT is coated with Pt, electrically connected to ground. An electric field is generated through the PZT substrate by applying a potential difference between an electrode on the top surface and the ground electrode. (b) Schematic of the multiferroic heterostructure, which consists of the PZT substrate with patterned electrodes, planarization layer, ground layer, and an array of Ni nanodisks. Inset 1: Detailed configuration of Ni disks in the center of the electrodes. Inset 2: SEM image of Ni disks with thickness of 15 nm and diameter of 400 nm (c) Cross-section drawing of the multiferroic heterostructure. (d) Image of the sample in a chip carrier. (e) Generation of anisotropic strain with an application of electric field on one electrode pair. Anisotropic in-plane strain is generated by applying a voltage on one underlying electrode pair (the active electrode pair is highlighted in orange color) and grounding the rest of the electrodes and the bottom ground layer. (For interpretation of the references to colour in this figure legend, the reader is referred to the web version of this article.)

surface electrodes. As opposed to the thin film PZTs in previous studies [28–30], the bulk substrates allow a larger dimension of surface electrodes that generates a more uniform strain near a substantially larger center area. The larger central strained area makes possible control and observation of multiple SD states at the same time, by placing multiple disks in this center area. Lastly, the eight surface patterned electrodes induce in-plane orthogonal strains every 45°, which apply the maximum magnetoelastic effective field to SD state at each strain application step.

Fabricating surface electrodes and Ni nanodisks on PZT substrates and characterizing their magnetic states present two crucial challenges. First, the PZT substrate has average surface roughness of 2.83 nm with peak roughness greater than 20 nm, attributed to the presence of polycrystalline grains [34]. The rough surface could cause magnetic pinning in thin film magnetic structures, impeding reorientation of the SD state. Second, the exposed surface electrodes cause issues with measurement. The exposed surface electrode emits stray electric fields, which might affect electric-field-sensitive micromagnetic measurements such as X-ray photoemission electron microscopy (X-PEEM), magnetic force microscopy (MFM), and scanning electron microscopy with polarization analysis (SEMPA). For MFM, the measurement method used here, stray electric fields impose electrostatic force on a MFM tip, altering the movement of the tip.

In order to overcome the problems of surface roughness and stray electric fields, we add a planarization layer to flatten the surface of the PZT substrate and a top grounding layer to shield the stray electric fields. After patterning electrodes on a PZT substrate, we deposit a 3 μm thick benzocyclobutene (BCB) layer as an insulator and planarization layer and then pattern a 5 nm Al/5 nm Ti/50 nm thick Pt plane (radius of 3 mm) as a top grounding plane (Fig. 3b). Details about the planarization with BCB and the fabrication process are given in Supplement S1 and S3, respectively. The Pt layer provides a ground plane to shield stray electric field for stable measurement. On top of the Pt layer, an array of 15 nm thick, 400 nm diameter Ni disks is fabricated in the center of the underlying electrodes by electron beam lithography (Fig. 3c).

In this multiferroic heterostructure, in-plane orthogonal strain is generated and transferred to the Ni disks, as described in the following (Fig. 3e). In-plane orthogonal strain on the PZT is induced by applying a voltage between a pair of opposing electrodes while grounding the rest of the electrodes and the bottom of the PZT substrate. Due to the different polarity of piezoelectric charge constants of PZT ($d_{33} > 0$ and d_{31}, $d_{32} < 0$), the region under the active electrodes expands in the out-of-plane direction ($s_z > 0$) and contracts in in-plane ($s_x, s_y < 0$). This mechanical contraction stretches the middle area between the active electrodes ($s_x > 0$) and contracts in the normal direction ($s_y < 0$), generating in-plane orthogonal strain. This in-plane strain is effectively transferred to the Ni disks through the BCB/Pt layers because the stacks of PZT/BCB/Pt layers form a composite laminate with a high volume fraction of PZT substrate and the deformation is loaded parallel to the in-plane direction (an isostrain condition [35]). In addition, the continuous Pt layer (E = 168 GPa) serves as a strain transfer layer between the soft BCB layer (E = 2.9 GPa) and the stiff Ni disks (E = 200 GPa), minimizing the shear lag in the Ni disks. By sequentially applying voltage to each of the electrode pairs, stepping orthogonal in-plane strains can be generated in steps of 45° in the center "sweet spot", where all the extrapolated electrodes meet. The electrically generated strains are transferred to the array of the Ni disks in the center area and reorient SD state in new easy axis. Ni has a negative saturation magnetostriction ($\lambda_s = -34$ppm) and creates easy axis along compressive strain. Therefore, a SD state in the Ni disks reorients toward the direction of compressive strain.

We first characterize the strain response in the multiferroic heterostructure using a finite element model (see Appendix: 1. Piezoelectric response). Fig. 4a shows the schematic of the multiferroic heterostructures without Ni disks. Eight Pt surface electrodes, 60 nm thick, are defined on a 300 μm thick PZT substrate (see Supplement S4 for the piezoelectric coefficient of PZT 620HD). The geometries of the electrodes are pre-determined by the same finite element simulation (see Supplement S2). The width of the electrode is 18 μm, and the distance between the electrode pairs is 60 μm (Fig. 4b). On top of the electrodes and the PZT substrate, layers of 3.0 μm thick BCB and 60 nm thick Pt are patterned. A voltage is applied to one electrode pair (highlighted in Fig. 4b), and the rest of the electrodes and the bottom side of the PZT are grounded. Grounding the electrodes affects the electric field distribution near the active electrodes but is seen as an acceptable tradeoff for avoiding charging, and the corresponding time-varying strain, that might occur with floating electrodes. In Fig. 4c, the strain response on the top Pt surface is calculated by averaging strains in the center 15 μm × 15 μm area, where Ni disks are fabricated. At 1.33 MV/m (400 V across a 300 μm thick PZT substrate), the center area of interest experiences a + 90 ppm of tensile strain ($s_x > 0$) along the active electrodes (standard deviation, $\sigma_x = 1.70$ ppm), and −100 ppm of compressive strain ($s_y < 0$) normal to the active electrodes (standard deviation, $\sigma_y = 3.91$ ppm). The strain profiles in the x and y axis at 1.33 MV/m are shown Fig. 4d and e. The average differential strain, $s_x - s_y$, at 1.33 MV/m is +190 ppm, as presented in Fig. 4f. By ramping up a voltage on the other electrode pair and grounding the rest of the surface electrodes and the bottom electrode, symmetric, in-plane orthogonal strains with respect to the new active electrode pair are observed. Therefore, four different in-plane orthogonal strains can be generated by applying a voltage to one of the four electrode pairs and grounding the rest: compressive strain along 0°/180°, 45°/225°, 90°/270°, and 135°/315° and tensile strain perpendicular to the compressive strain.

The magnetoelastic behavior in Ni disks with thickness of 15 nm and diameter of 400 nm is predicted by the following micromagnetic/elastodynamic simulation [36] (see Appendix: 2. Magnetoelastic response) that couples the electrically generated strains with SD states in the disks. The four different orthogonal strains with 1.33 MV/m that are obtained from the previous finite element model are sequentially applied to the Ni disk. In Fig. 5a', prior to the strain application, an initial SD state is created in the Ni disk after saturating the Ni disk magnetization in the +x axis. Then, the first anisotropic strain that is created by applying a voltage to the A-A' pair (Fig. 5b). The anisotropic strain induces a new easy axis in the direction of compressive strain, +45°, reorienting the magnetization toward the easy axis. After releasing the strain, the exchange interaction work in cooperation with the demagnetization field to form the stable SD state in 45° (Fig. 5b'). In Fig. 5c'–e', further rotations are shown with different stain application steps and removal. After the FEA simulations, we fabricate the multiferroic heterostructures (see Supplement S3 for the detailed fabrication process) and experimentally measure the step-wise 180° rotation of the SD state by MFM. Prior to the MFM measurement, a 3 kOe of external magnetic field is applied to 15 nm thick, 400 nm OD Ni disks to create a SD state along the x-axis. Fig. 5a'' MFM shows the initial SD state in two Ni disks before a voltage is applied. Due to risks of electrical breakdown in the MFM system, each MFM image in Fig. 5b''–e'' is measured after applying 400 V from outside of the MFM. Fig. 5b'' shows the rotation of SD state toward 45°/225° after applying first orthogonal strains generated by A-A' pair. In Fig. 5c''–e'', the SD states align with 90°/270°, 135°/315°, and 180°/0° corresponding with a series of voltage applications on the remaining electrode pairs (B-B', C-C', and
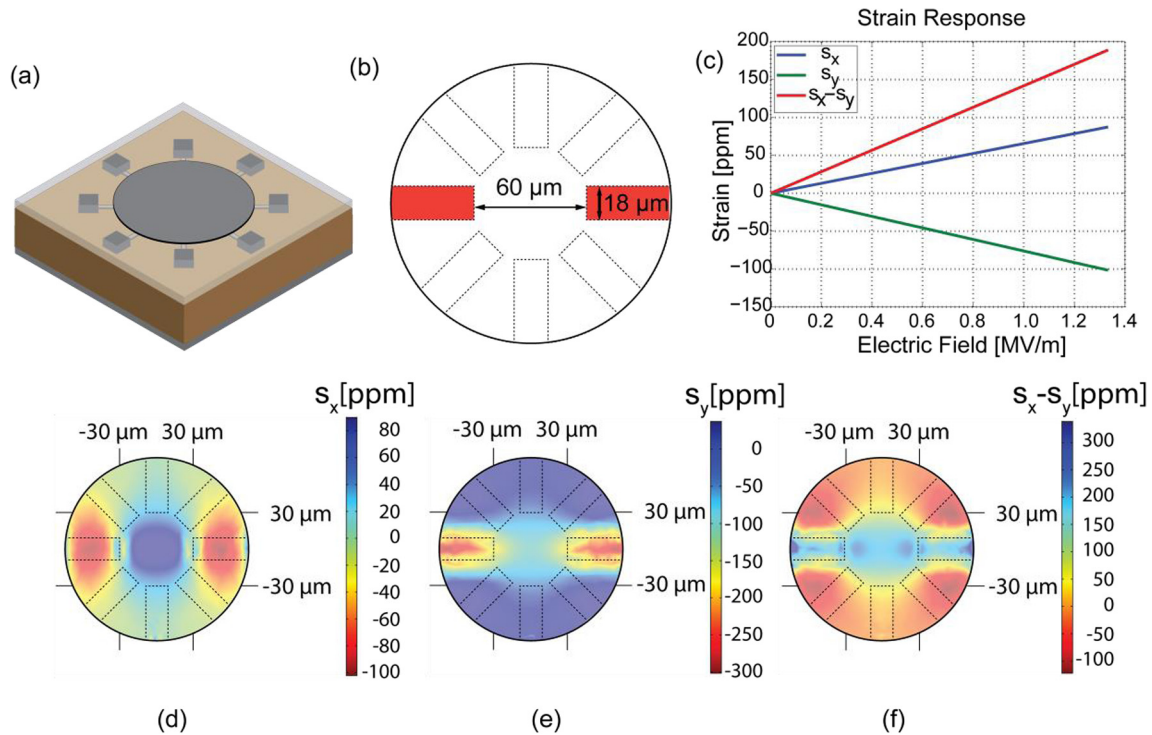
Fig. 4. Finite element analysis: strain response of the multiferroic heterostructure with a voltage applied. (a) Schematic of the multiferroic heterostructure. (b) Electrode geometry. The electrodes that have a voltage applied are highlighted in red. (c) Average strain response of the center area, 15 μm × 15 μm, with an electric field. (d) Strain profile in the x axis at 1.33 MV/m (e) Strain profile in the y axis at 1.33 MV/m (f) Differential strain profile at 1.33 MV/m. (For interpretation of the references to colour in this figure legend, the reader is referred to the web version of this article.)
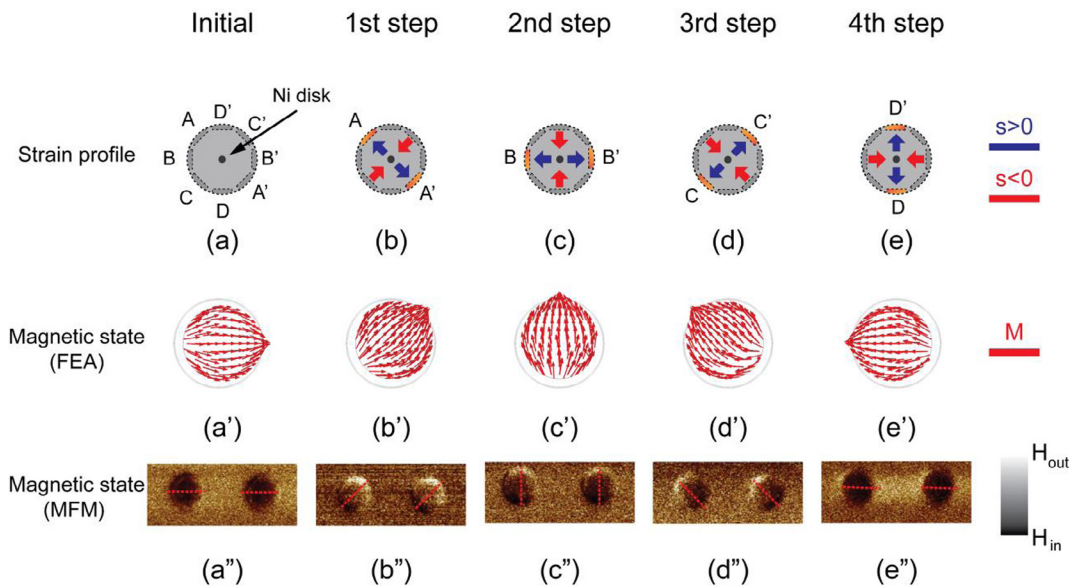
Fig. 5. Finite element analysis and MFM results of magnetoelastic response in Ni disks with thickness of 15 nm and diameter of 400 nm. (a)–(e) strain configuration with sequential voltage application steps (a′)–(e′) FEA simulation results of magnetoelastic responses in the Ni disk. (M represents magnetization) (a″)–(e″) MFM results of two Ni disks as strain is applied. (H_{in} and H_{out} nominally represent stray magnetic field coming in and out from the disks, respectively. See Supplement S4 for further information regarding MFM interpretation.)

D-D′, respectively) (see Supplement S4 for the detailed MFM interpretation). Although FEA simulations predict full 360° rotation, we were unable to observe further rotations in the two disks after the 180° rotation. We hypothesize two factors that impeded the further rotation over 180°. First, the coupling of the magnetic MFM tip with the Ni disks alters the magnetic state in the Ni disks. We use low-momentum MFM tips (MESP-LM-V2 from Bruker) to minimize the magnetic interruption of magnetic state, but undesired interactions are still observed during measurement. Therefore, it is possible that the MFM tip disrupted the magnetic state of the disk into a state that was not easily rotated. Second, we note that in general stepping rotations of SD states are observed in most of the disks. However, some of the SD states either fall in multi-domain state/vortex states, or show no further rotation after

several steps of strain applications. We hypothesize these issues could be caused by magnetic domain pinning due to surface and edge roughness. Future work can be done with non-invasive measurements, such as photoemission electron microscopy (PEEM) and scanning electron microscopy with polarization analysis (SEMPA) to mitigate any concerns about unwanted interactions from magnet-based measurement techniques.

4. Conclusion

In summary, we have demonstrated multi-step rotation of the SD state in Ni nanodisks using multiferroic magnetoelastic coupling. The generation of multi-directional piezoelectric strains with surface patterned electrodes and the magnetoelastic behavior in the nanodisks are predicted by fully coupled multi-physics finite elements simulations. The experimental results show deterministic rotation of the SD state in agreement with the simulation results. This new multiferroic approach to control of magnetism solely by electric field could open new ways to locally control magnetism at the nanoscale without the scaling limit imposed by Joule heating.

Acknowledgments

Appendix A

A.1. Finite element analyses

Due t the large discrepancy in the element size of the Ni disks and the piezoelectric structure, the finite element analyses simulation consists of two steps: 1. calculation of mechanical displacement (piezeoelectric response); 2. calculation of magnetic equilibrium with the mechanical displacement (magnetoelastic response).

1. Piezoelectric response

The finite element model of the piezoelectric structure with a 300 µm thick PZT substrate, 60 nm thick eight Pt electrodes, 3 µm thick BCB layer, and 60 nm thick Pt ground plane is defined in COMOL Multiphysics. The piezoelectric response of the PZT substrate is calculated by the piezoelectric constitutive equations: strain-charge form as

$$S = s_E \cdot T + d^T \cdot E \tag{3}$$

$$D = d \cdot T + \varepsilon_E \cdot E \tag{4}$$

where S is the strain, T is the stress, E is the electric field, and D is the electric displacement field, s_E is the material compliance, d is the piezoelectric coupling coefficient, and ε_E is the electric permittivity. The piezoelectric constants of PZT 610HD are given in Supplement S5. The generated piezoelectric strain is transferred through the BCB layer and the Pt ground layer. We assume that the BCB and the Pt are linear elastic materials and solve for linear elasticity to characterize the surface strain response. Four cases of the mechanical deformation are obtained by sequentially applying voltage to the four electrode pairs.

2. Magnetoelastic response

The dynamics of magnetization follows in a 15 nm thick, 400 nm OD Ni disk by Landau-Lifshitz-Gilbert (LLG) equation:

$$\frac{\partial \vec{M}}{\partial t} = -\mu_0 \gamma \vec{M} \times \vec{H}_{eff} + \alpha \left(\vec{M} \times \frac{\partial \vec{M}}{\partial t} \right) \tag{5}$$

where μ_0 is the permeability of free space, γ is the Gilbert gyromagnetic ratio, α is the Gilbert damping constant, and $\vec{M}$ is the normalized magnetization. In this study, we assume no external magnetic field and magnetocrystalline anisotropy. Therefore, the total effective magnetic field, $\vec{H}_{eff}$, includes the exchange effective field ($\vec{H}_{ex}$), demagnetization effective field ($\vec{H}_d$), and magnetoelastic effective field ($\vec{H}_{me}$). The demagnetization field is calculated from the gradient of the magnetic potential, the exchange field from the exchange energy, and the magnetoelastic field from the magnetoelastic energy. The magnetoelastic energy is calculated based on the loaded mechanical displacement on the Ni disk that is calculated from the piezoelectric response. COMSOL multi-physics solves the weak form of LLG equations and finds the equilibrium state [36].

Appendix B. Supplementary data

Supplementary data (additional information regarding planarization of PZT surface, calculation of optimal electrode configuration for 300 µm thick PZT substrate, fabrication process, and piezoelectric coefficients of PZT 610HD) associated with this article can be found, in the online version, at http://dx.doi.org/10.1016/j.jmmm.2017.04.077.

References

[1] M. Bibes, A. Barthélémy, Towards a magnetoelectric memory, Nat. Mater. (2008) 425–426.
[2] K. Wang, J.-M. Liu, Z. Ren, Multiferroicity: the coupling between magnetic and polarization orders, Adv. Phys. 58 (2009) 321–448.
[3] I. De Vlaminck, C. Dekker, Recent advances in magnetic tweezers, Annu. Rev. Biophys. 41 (2012) 453–472.
[4] J. Dobson, Remote control of cellular behaviour with magnetic nanoparticles, Nat. Nanotechnol. 3 (2008) 139–143.
[5] A. Tay, F.E. Schweizer, D. Di Carlo, Micro-and nano-technologies to probe the mechano-biology of the brain, Lab Chip 16 (2016) 1962–1977.
[6] C. Murray, E. Pao, P. Tseng, S. Aftab, R. Kulkarni, M. Rettig, D. Di Carlo, Quantitative magnetic separation of particles and cells using gradient magnetic ratcheting, Small 12 (2016) 1891–1899.
[7] P. Tartaj, M. del Puerto Morales, S. Veintemillas-Verdaguer, T. González-Carreño, C.J. Serna, The preparation of magnetic nanoparticles for applications in biomedicine, J. Phys. D Appl. Phys. 36 (2003) R182.
[8] R. Hao, R. Xing, Z. Xu, Y. Hou, S. Gao, S. Sun, Synthesis, functionalization, and biomedical applications of multifunctional magnetic nanoparticles, Adv. Mater. 22 (2010) 2729–2742.
[9] D. Niarchos, Magnetic MEMS: key issues and some applications, Sens. Actuators, A 109 (2003) 166–173.
[10] T.M. Liakopoulos, C.H. Ahn, A micro-fluxgate magnetic sensor using micromachined planar solenoid coils, Sens. Actuators, A 77 (1999) 66–72.
[11] E. Rapoport, D. Montana, G. Beach, Integrated capture, transport, and magneto-mechanical resonant sensing of superparamagnetic microbeads using magnetic domain walls, Lab Chip 12 (2012) 4433–4440.
[12] W. Eerenstein, N.D. Mathur, J.F. Scott, Multiferroic and magnetoelectric materials, Nature 442 (2006) 759–765.
[13] N.A. Spaldin, M. Fiebig, The renaissance of magnetoelectric multiferroics, Science 309 (2005) 391–392.
[14] R. Ramesh, N.A. Spaldin, Multiferroics: progress and prospects in thin films, Nat. Mater. 6 (2007) 21–29.
[15] J. Ma, J. Hu, Z. Li, C.W. Nan, Recent progress in multiferroic magnetoelectric composites: from bulk to thin films, Adv. Mater. 23 (2011) 1062–1087.
[16] J.M. Hu, L.Q. Chen, C.W. Nan, Multiferroic heterostructures integrating ferroelectric and magnetic materials, Adv. Mater. 28 (2016) 15–39.
[17] M. Buzzi, R. Chopdekar, J. Hockel, A. Bur, T. Wu, N. Pilet, P. Warnicke, G. Carman, L. Heyderman, F. Nolting, Single domain spin manipulation by electric fields in strain coupled artificial multiferroic nanostructures, Phys. Rev. Lett. 111 (2013) 027204.

[18] J.L. Hockel, A. Bur, T. Wu, K.P. Wetzlar, G.P. Carman, Electric field induced magnetization rotation in patterned Ni ring/Pb (Mg1/3Nb2/3) O3](1–0.32)-[PbTiO3] 0.32 heterostructures, Appl. Phys. Lett. 100 (2012) 022401.

[19] H. Ahmad, J. Atulasimha, S. Bandyopadhyay, Reversible strain-induced magnetization switching in FeGa nanomagnets: pathway to a rewritable, non-volatile, non-toggle, extremely low energy straintronic memory, Sci. Rep. 5 (2015).

[20] C.-W. Nan, M.I. Bichurin, S. Dong, D. Viehland, G. Srinivasan, Multiferroic magnetoelectric composites: historical perspective, status, and future directions, J. Appl. Phys. 103 (2008) 031101.

[21] V. Sampath, N. D'Souza, D. Bhattacharya, G.M. Atkinson, S. Bandyopadhyay, J. Atulasimha, Acoustic-wave-induced magnetization switching of magnetostrictive nanomagnets from single-domain to nonvolatile vortex states, Nano Lett. 16 (2016) 5681–5687.

[22] N. D'Souza, M.S. Fashami, S. Bandyopadhyay, J. Atulasimha, Experimental clocking of nanomagnets with strain for ultralow power Boolean logic, Nano Lett. 16 (2016) 1069–1075.

[23] H. Sohn, M.E. Nowakowski, C.-Y. Liang, J.L. Hockel, K. Wetzlar, S. Keller, B.M. McLellan, M.A. Marcus, A. Doran, A. Young, Electrically driven magnetic domain wall rotation in multiferroic heterostructures to manipulate suspended on-chip magnetic particles, ACS Nano 9 (2015) 4814–4826.

[24] J.L. Hockel, S.D. Pollard, K.P. Wetzlar, T. Wu, Y. Zhu, G.P. Carman, Electrically controlled reversible and hysteretic magnetic domain evolution in nickel film/Pb(Mg1/3Nb2/3)O3]0.68-[PbTiO3]0.32 (011) heterostructure, Appl. Phys. Lett. 102 (2013) 242901.

[25] T. Wu, P. Zhao, M. Bao, A. Bur, J.L. Hockel, K. Wong, K.P. Mohanchandra, C.S. Lynch, G.P. Carman, Domain engineered switchable strain states in ferroelectric (011) [Pb(Mg1/3Nb2/3)O3](1 − x)-[PbTiO3]x (PMN-PT, x ≈ 0.32) single crystals, J. Appl. Phys. 109 (2011) 124101.

[26] S.-E. Park, T.R. Shrout, Ultrahigh strain and piezoelectric behavior in relaxor based ferroelectric single crystals, J. Appl. Phys. 82 (1997) 1804–1811.

[27] J. Cui, J.L. Hockel, P.K. Nordeen, D.M. Pisani, C.-Y. Liang, G.P. Carman, C.S. Lynch, A method to control magnetism in individual strain-mediated magnetoelectric islands, Appl. Phys. Lett. 103 (2013) 232905.

[28] C.-Y. Liang, A.E. Sepulveda, D. Hoff, S.M. Keller, G.P. Carman, Strain-mediated deterministic control of 360° domain wall motion in magnetoelastic nanorings, J. Appl. Phys. 118 (2015) 174101.

[29] J.-M. Hu, T. Yang, K. Momeni, X. Cheng, L. Chen, S. Lei, S. Zhang, S. Trolier-McKinstry, V. Gopalan, G.P. Carman, Fast magnetic domain-wall motion in a ring-shaped nanowire driven by a voltage, Nano Lett. 16 (2016) 2341–2348.

[30] J. Cui, C.-Y. Liang, E.A. Paisley, A. Sepulveda, J.F. Ihlefeld, G.P. Carman, C.S. Lynch, Generation of localized strain in a thin film piezoelectric to control individual magnetoelectric heterostructures, Appl. Phys. Lett. 107 (2015) 092903.

[31] M. Donahue, D. Porter, Oommf user's guide, version 1.0, interagency report nistir 6376, National Institute of Standards and Technology, Gaithersburg, MD, 1999.

[32] T. Wren, B. Gribkov, V. Petrashov, O. Kazakova, Phase diagram of magnetic states in nickel submicron disks, J. Appl. Phys. 118 (2015) 023906.

[33] G. Herzer, Nanocrystalline soft magnetic materials, J. Magn. Magn. Mater. 112 (1992) 258–262.

[34] C. Wang, Investigation of Sputtered Ferroelectric Thin Films on Silicon Substrates, Carnegie Mellon University, PA, 2007.

[35] W.D. Callister, D.G. Rethwisch, Materials Science and Engineering: An Introduction, Wiley, New York, 2007.

[36] C.-Y. Liang, S.M. Keller, A.E. Sepulveda, A. Bur, W.-Y. Sun, K. Wetzlar, G.P. Carman, Modeling of magnetoelastic nanostructures with a fully coupled mechanical-micromagnetic model, Nanotechnology 25 (2014) 435701.